

# Theoretical investigation of thermoelectric transport properties of cylindrical Bi nanowires

Yu-Ming Lin,<sup>1</sup> Xiangzhong Sun,<sup>2</sup> and M. S. Dresselhaus<sup>1,2,\*</sup>

<sup>1</sup>*Department of Electrical Engineering and Computer Science, Massachusetts Institute of Technology, Cambridge, Massachusetts 02139-4307*

<sup>2</sup>*Department of Physics, Massachusetts Institute of Technology, Cambridge, Massachusetts 02139-4307*

(Received 7 March 2000)

We report here a theoretical model for the transport properties of cylindrical Bi nanowires. Based on the band structure of Bi nanowires and the semiclassical transport model, the thermoelectric figure of merit  $Z_{1D}T$  is calculated for Bi nanowires with various wire diameters and wire orientations. The results show the trigonal axis is the most favorable wire orientation for thermoelectric applications, and  $Z_{1D}T > 1$  is predicted for  $n$ -type trigonal wires with diameters  $d_w < 10$  nm. The effect of the  $T$ -point holes on  $Z_{1D}T$  is also investigated. It is found that  $Z_{1D}T$  can be significantly enhanced, especially for  $p$ -type Bi nanowires, if the  $T$ -point holes are removed or suppressed.

## I. INTRODUCTION

Nanowire systems have attracted a great deal of research interest because they allow study of quasi-one-dimensional (1D) quantum systems<sup>1,2</sup> and offer potential applications in thermoelectrics.<sup>3</sup> Bi, which is a semimetal with one anisotropic hole pocket at the  $T$  point of the Brillouin zone and three highly anisotropic and nonparabolic electron ellipsoids at the  $L$  points, is especially favorable for studying low-dimensional systems and for thermoelectric applications, due to its small electron effective mass and the highly anisotropic Fermi surface. The detailed crystal and electronic band structure of bulk Bi are given in Refs. 4–6. Recently, substantial progress has been made in synthesizing single-crystal Bi nanowire arrays in anodic alumina templates with wire diameters ranging from 7 nm to 200 nm.<sup>7–10</sup> From x-ray diffraction studies, it was found that these Bi nanowires possess a preferred growth direction along the wire axis: the  $[01\bar{1}2]$  direction for smaller wire diameter nanowires ( $d_w \leq 50$  nm) and the  $[10\bar{1}1]$  direction for larger diameter nanowires ( $d_w \geq 60$  nm).<sup>7,8,11</sup> In previous theoretical modeling studies,<sup>12,13</sup> a significant enhancement of the thermoelectric performance with  $Z_{1D}T > 1$  was predicted for Bi nanowires with wire diameters  $d_w < 10$  nm.<sup>13</sup>

To model the electronic structure of a nanowire system, a simple assumption is usually made for an ideal 1D quantum wire, where the carriers are confined inside a cylindrical potential well with an infinite potential height. An extension of this simple approach provides a good approximation for Bi nanowires embedded in an alumina template, in view of the large band gap ( $\sim 3.2$  eV) of the anodic alumina template material, which provides excellent confinement for the carriers in the embedded quantum wires.

Since the electron motion in the quantum wires is restricted in directions normal to the wire axis, the quantum confinement causes the energies associated with the in-plane motion to be quantized, and the lowest energy level is, roughly speaking, given by

$$\Delta E \sim \frac{\pi^2 \hbar^2}{m_p^* d_w^2}, \quad (1)$$

where  $m_p^*$  is the average in-plane effective mass of the electrons and  $d_w$  is the wire diameter. Since the motion along the wire axis is not restricted, the electrons would have a dispersion relation for small  $k_l$  that looks like

$$E_{nm}(k_l) = \varepsilon_{nm} + \frac{\hbar^2 k_l^2}{2m_l^*}, \quad (2)$$

where  $\varepsilon_{nm}$  represents the quantized energy level (at  $k_l=0$ ) labeled by two quantum numbers ( $n, m$ ), and  $k_l$  and  $m_l^*$  are the wave vector of the electron wave functions and the effective mass for electrons traveling along the wire axis, respectively. We note that for materials such as Bi with highly anisotropic carrier pockets, the effective mass  $m_p^*$ , which determines the subband edge energies  $\varepsilon_{nm}$ , can be very different from the mass  $m_l^*$ , which characterizes the electron motion along the wire.

In the nanowire system, the quantized subband energy  $\varepsilon_{nm}$  and the transport effective mass  $m_l^*$  along the wire axis are the two most important parameters that determine almost every electronic property of this 1D system. However, due to the special geometric configuration of Bi nanowires (long circular wires with a high aspect length/diameter ratio) and the anisotropic carrier pockets in Bi, the exact calculation of the band structure in Bi nanowires was found to be very challenging, and several approximation methods have been used to study the electronic band structures of Bi nanowires in previous theoretical models. In the first calculation carried out by Zhang *et al.*,<sup>12,14</sup> the quantized energy levels were evaluated by using a cyclotron effective mass approximation for the in-plane effective mass perpendicular to the wire axis:

$$m_p^* \approx m_c^* = \left( \frac{\det \mathbf{M}_e}{\hat{\mathbf{I}} \cdot \mathbf{M}_e \cdot \hat{\mathbf{I}}} \right)^{1/2}, \quad (3)$$

where  $\hat{\mathbf{I}}$  is the unit vector along the wire axis and  $\mathbf{M}_e$  is the effective mass tensor. The transport effective mass was approximated by

$$m_l^* \approx \hat{\mathbf{I}} \cdot \mathbf{M}_e \cdot \hat{\mathbf{I}}. \quad (4)$$

In the earliest models,<sup>14</sup> parabolic dispersion relations were assumed for both electrons and holes. With these simplifying approximations, the quantized energy levels could be readily derived by solving the 2D Schrödinger equation with a circular boundary condition.<sup>14</sup> However, the cyclotron effective mass approximation is an oversimplification for the in-plane effective mass, and is not valid for electrons with a highly anisotropic in-plane effective mass tensor. Instead of  $m_c^* = \sqrt{m_1 m_2}$  for the average in-plane effective mass  $m_p^*$ , where  $m_1$  and  $m_2$  are the two principal mass components in the plane normal to the wire axis, the quantized energy states  $\varepsilon_{nm}$  are to a much closer approximation determined by  $m_p^*$  given by (as will be shown later)

$$\frac{1}{m_p^*} \approx \frac{1}{2} \left( \frac{1}{m_1} + \frac{1}{m_2} \right). \quad (5)$$

The discrepancies between  $m_c^*$  and  $m_p^*$  can be very significant if  $m_1$  and  $m_2$  are very different, as they are for Bi.

Subsequently, an improved model to describe the electronic states in Bi nanowires was developed by Sun *et al.*,<sup>13,15</sup> based on the square wire approximation for wires oriented along the three principal axes. With the edges of the square cross-section chosen to be parallel to the principal axes of the in-plane mass tensor for each carrier pocket, the square boundary condition greatly simplified the eigenvalue problem for solving the Schrödinger equation and yielded analytical solutions for the quantized energy levels. In this approximation, the transport effective mass along the wire axis was derived as

$$m_i^* = (\hat{\mathbf{i}} \cdot \mathbf{M}_e^{-1} \cdot \hat{\mathbf{i}})^{-1} \quad (6)$$

for a parabolic carrier pocket. Although the square wire approximation provided a better solution for the in-plane effective masses and for the quantized energy states  $\varepsilon_{nm}$  than the previous cyclotron effective mass approximation, further improvements are needed to describe the actual *circular* wires used in the experiment and their proper symmetries, which require that the physical quantities should be invariant under rotations about the wire axis. In the square wire approximation, the quantized subband energies are highly dependent on the rotations of the square cross section about the wire axis, and therefore the subband energies are not well defined in this approximation.

In this paper, we present a theoretical model for Bi nanowires, which explicitly takes into account the cylindrical wire boundary conditions, the anisotropic carrier effective mass tensor, i.e., nonparabolic features of the *L*-point conduction and valence bands, and the multiple carrier pockets. The temperature dependence of the band structure of Bi was also considered to obtain a more realistic result for the temperature-dependent transport phenomena. A numerical method was designed to derive the quantized subband energies and the electronic wave functions of the circular wire. In addition, the ambiguity between the two different expressions of Eqs. (4) and (6) for the 1D transport effective mass in previous models is clarified in the present work. Using the electronic band structure of Bi nanowires thus obtained, a semiclassical transport model, which is based on the Boltzmann transport equation for 1D systems, is then developed

and is used to study the thermoelectric properties of the unique Bi nanowire system for various wire orientations, including the three principal axes and the two preferred growth directions at 77 K, which is a temperature of great interest for cryogenic cooling applications. The results show that the thermoelectric performance strongly depends on the wire diameter and the wire orientation, with the trigonal orientation being the most favorable direction. The effect of the *T*-point holes on the thermoelectric performance is also discussed. It is found that the thermoelectric performance can be greatly improved, especially for *p*-type wires, if the *T*-point holes are removed or suppressed, as, for example, by adding appropriate concentrations of Sb.<sup>16</sup>

Transport measurements of Bi nanowire arrays of different diameters and carrier concentrations have been performed,<sup>10,12,14,17-19</sup> and the experimental results are qualitatively consistent with the predictions from our theoretical models. A detailed comparison between the theoretical and the experimental results is given in Ref. 11.

## II. ELECTRONIC BAND STRUCTURE OF BI NANOWIRES

### A. Theoretical modeling

For an infinitely long wire with a circular cross section of diameter  $d_w$ , we take the  $z'$  axis to be parallel to the wire axis with the  $x'$  and  $y'$  axes lying on the cross-sectional plane. Since the wire axis is allowed to be oriented along an arbitrary direction with respect to the crystallographic directions, the inverse effective mass tensor of one of the carrier pockets in the wire coordinates  $(x', y', z')$  has the general form

$$\boldsymbol{\alpha} \equiv \mathbf{M}^{-1} = \begin{pmatrix} \alpha_{11} & \alpha_{12} & \alpha_{13} \\ \alpha_{21} & \alpha_{22} & \alpha_{23} \\ \alpha_{31} & \alpha_{32} & \alpha_{33} \end{pmatrix}, \quad (7)$$

where  $\alpha_{ij} = \alpha_{ji}$ .

Without loss of generality, we first seek solutions for the *T*-point holes, which can be well described by a parabolic dispersion relation, in order to illustrate the numerical methods developed in the next section. Solutions for the *L*-point carriers with nonparabolic dispersion relations are discussed in Sec. II C. The envelope wave function  $\Psi(\mathbf{r}')$  of the *T*-point holes is governed by the effective-mass Schrödinger equation<sup>20</sup>

$$-\frac{\hbar^2}{2} \nabla \cdot \boldsymbol{\alpha} \cdot \nabla \Psi(\mathbf{r}) = E \Psi(\mathbf{r}). \quad (8)$$

The cylindrical symmetry properties of the circular wire are then used to simplify Eq. (8). By a proper rotation about the  $z'$  axis, it is possible to make the matrix elements  $\alpha_{12} = \alpha_{21} = 0$ , and Eq. (8) can then be written as

$$\begin{aligned} & \alpha_{11} \frac{\partial^2 \Psi}{\partial x'^2} + \alpha_{22} \frac{\partial^2 \Psi}{\partial y'^2} + 2\alpha_{13} \frac{\partial^2 \Psi}{\partial x' \partial z'} + 2\alpha_{23} \frac{\partial^2 \Psi}{\partial y' \partial z'} + \alpha_{33} \frac{\partial^2 \Psi}{\partial z'^2} \\ & = \left( -\frac{2E}{\hbar^2} \right) \Psi. \end{aligned} \quad (9)$$

Since the electrons are unbounded in the  $z'$  direction, we assume that the electron wave function  $\Psi(\mathbf{r}')$  takes the form:

$$\Psi(\mathbf{r}') = u(x, y) \exp(i\xi x') \exp(i\eta y') \exp(ik_{z'} z'), \quad (10)$$

where  $\xi$  and  $\eta$  are constants to be determined, and  $k_{z'}$  is the wave number of the traveling wave in the  $z'$  direction. We note that by letting  $\xi = -\alpha_{13}/\alpha_{11}k_{z'}$  and  $\eta = -\alpha_{23}/\alpha_{22}k_{z'}$ , the coupling terms between  $x', y'$ , and  $k_{z'}$  are eliminated, and Eq. (9) is reduced to a simple second-order differential equation in  $x'$  and  $y'$  only:

$$-\frac{\hbar^2}{2} \left( \alpha_{11} \frac{\partial^2}{\partial x'^2} + \alpha_{22} \frac{\partial^2}{\partial y'^2} \right) u = \left( E - \frac{\hbar^2 k_{z'}^2}{2m_{33}} \right) u \quad (11)$$

where

$$m_{33} \equiv \left( \alpha_{33} - \frac{\alpha_{23}^2}{\alpha_{22}} - \frac{\alpha_{13}^2}{\alpha_{11}} \right)^{-1} = \hat{\mathbf{z}}' \cdot \mathbf{M} \cdot \hat{\mathbf{z}}'. \quad (12)$$

Equation (11) is reminiscent of a 2D Schrödinger equation with in-plane effective mass components

$$\begin{aligned} m_{x'} &\equiv \alpha_{11}^{-1} = (\hat{\mathbf{x}}' \cdot \mathbf{M}^{-1} \cdot \hat{\mathbf{x}}')^{-1}, \\ m_{y'} &\equiv \alpha_{22}^{-1} = (\hat{\mathbf{y}}' \cdot \mathbf{M}^{-1} \cdot \hat{\mathbf{y}}')^{-1}, \end{aligned} \quad (13)$$

in the  $x'$  and  $y'$  directions, respectively. Since  $u(x', y')$  must satisfy the same boundary condition as  $\Psi(\mathbf{r})$  according to Eq. (10):  $u(x', y') \equiv 0$  when  $x'^2 + y'^2 = (d_w/2)^2$ , the eigenvalues of  $u(x', y')$  in Eq. (11) are quantized, and the energy of the electrons is written as

$$E_{nm}(k_{z'}) = \varepsilon_{nm} + \frac{\hbar^2 k_{z'}^2}{2m_{33}}, \quad (14)$$

where  $\varepsilon_{nm}$  is the eigenvalue of Eq. (11) corresponding to the subband edge eigenstate at  $k_{z'} = 0$  labeled by the quantum numbers  $(n, m)$ . In Eq. (14), we see that the electron states split into many subbands with band edges at  $E = \varepsilon_{nm}$ , and each subband behaves like a 1D system in the  $z'$  direction with the transport effective mass  $m_{z'} = m_{33}$ . It should be noted that since only the cylindrical symmetry of the wire was actually assumed in the derivation of Eqs. (11)–(13), these results are also applicable to wires with a finite potential height. We also note that the effective masses  $m_{x'}$  and  $m_{y'}$  that determine the bound-state energies have different expressions from the transport effective mass  $m_{z'}$ , which characterizes the 1D dispersion relation, as indicated by Eqs. (12) and (13). In addition, compared to the exact expression, Eq. (12), for the transport effective mass  $m_{z'}$ , the transport effective mass in Eq. (4) used by the previous cyclotron effective mass approximation is a better approximation than the one in Eq. (6) for the square wire approximation.

### B. Numerical solutions

In Sec. II A, the quantized energies of the bound states of anisotropic carriers in an infinitely long circular wire are determined by the 2D differential equation, which can be rewritten as

$$\left( \alpha \frac{\partial^2}{\partial x^2} + \beta \frac{\partial^2}{\partial y^2} \right) u = -\lambda u, \quad (15)$$

where we let  $\alpha \equiv \alpha_{11}$ ,  $\beta \equiv \alpha_{22}$ , and

$$\lambda \equiv \frac{2}{\hbar^2} \left( E - \frac{\hbar^2 k_{z'}^2}{2m_{33}} \right). \quad (16)$$

Also, the dummy variables  $x', y'$  in Eq. (11) are here replaced by  $x, y$  for simplicity. For the special and simple case where  $\alpha = \beta$ , which only applies to the  $T$ -point hole pocket in trigonal Bi nanowires, the wavefunction of Eq. (15) has the analytic solution

$$u_{mn}(r) \sim J_m(\chi_{mn} r) e^{im\theta}, \quad (17)$$

where  $J_m$  is the  $m$ th Bessel function, and  $\chi_{mn}$  is the  $n$ th root of  $J_m(x d_w/2) = 0$  in order to satisfy the boundary conditions. The eigenvalue  $\lambda$  corresponding to the wavefunction in Eq. (17) is then given by  $\lambda_{mn} = \alpha \chi_{mn}^2$ .

For the general situation where  $\alpha \neq \beta$ , there are no analytic solutions and the eigenvalues can only be derived through numerical methods. In the following, numerical solutions to this particular eigenvalue problem are obtained by transforming the differential equation Eq. (15) into a corresponding difference equation, and the resulting Hamiltonian matrix can be solved numerically to high accuracy with the aid of computers.

First, due to the cylindrical boundary condition  $u(r = d_w/2) \equiv 0$ , it is advantageous to express Eq. (15) in terms of cylindrical coordinates:

$$\begin{aligned} \frac{\partial^2 u}{\partial x^2} &= \cos^2 \theta \frac{\partial^2 u}{\partial r^2} + 2 \frac{\cos \theta \sin \theta}{r^2} \frac{\partial u}{\partial \theta} - 2 \frac{\cos \theta \sin \theta}{r} \frac{\partial^2 u}{\partial r \partial \theta} \\ &\quad + \frac{\sin^2 \theta}{r} \frac{\partial u}{\partial r} + \frac{\sin^2 \theta}{r^2} \frac{\partial^2 u}{\partial \theta^2} \end{aligned} \quad (18)$$

$$\begin{aligned} \frac{\partial^2 u}{\partial y^2} &= \sin^2 \theta \frac{\partial^2 u}{\partial r^2} - 2 \frac{\cos \theta \sin \theta}{r^2} \frac{\partial u}{\partial \theta} + 2 \frac{\cos \theta \sin \theta}{r} \frac{\partial^2 u}{\partial r \partial \theta} \\ &\quad + \frac{\cos^2 \theta}{r} \frac{\partial u}{\partial r} + \frac{\cos^2 \theta}{r^2} \frac{\partial^2 u}{\partial \theta^2}, \end{aligned} \quad (19)$$

where  $\theta$  is the polar angle to the  $x$  axis, and  $r$  is the perpendicular distance to the  $z$  axis in cylindrical coordinates. To transform Eq. (15) into a difference equation, we create a mesh consisting of  $M$  concentric circles and  $N$  sectors within the wire cross section, as shown in Fig. 1. The polar coordinates of the  $M \times N$  grid points in this circular mesh are

$$(r_m, \theta_n) = (m \delta r, n \delta \theta), \quad (20)$$

$$m = 1, 2, \dots, M \quad n = 0, 1, \dots, (N-1)$$

where  $\delta r = d_w/2M$  and  $\delta \theta = 2\pi/N$  are, respectively, the distances between adjacent concentric circles and the angle spanned by each sector. With these assigned grid points, the derivatives at  $(r, \theta) = (r_m, \theta_n)$  in Eqs. (18) and (19) are approximated by

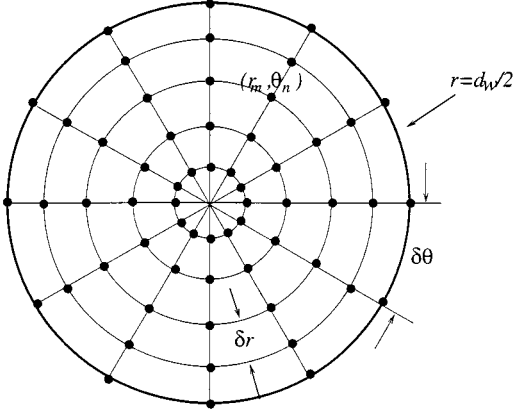


FIG. 1. Schematic diagram of the grid points used to transform each differential equation into a difference equation. The mesh in the circular wire cross section consists of  $M$  concentric circles and  $N$  sectors. In the figure above,  $M=5$  and  $N=12$ .

$$\frac{\partial u}{\partial r} \approx \frac{1}{2\delta r}(u_{m+1,n} - u_{m-1,n}), \quad (21)$$

$$\frac{\partial u}{\partial \theta} \approx \frac{1}{2\delta \theta}(u_{m,n+1} - u_{m,n-1}), \quad (22)$$

$$\frac{\partial^2 u}{\partial r^2} \approx \frac{1}{(\delta r)^2}(u_{m+1,n} + u_{m-1,n} - 2u_{m,n}), \quad (23)$$

$$\frac{\partial^2 u}{\partial \theta^2} \approx \frac{1}{(\delta \theta)^2}(u_{m,n+1} + u_{m,n-1} - 2u_{m,n}), \quad (24)$$

$$\frac{\partial^2 u}{\partial r \partial \theta} \approx \frac{1}{4(\delta \theta)(\delta r)}(u_{m+1,n+1} + u_{m-1,n-1} - u_{m+1,n-1} - u_{m-1,n+1}), \quad (25)$$

where  $u_{m,n} = u(r_m, \theta_n)$  is the value of the wave function  $u(r, \theta)$  taken at the grid point  $(r_m, \theta_n)$ . After substituting the derivatives in Eqs. (18) and (19) by their finite difference counterparts in Eqs. (21)–(25), we obtain a difference equation of  $u_{m,n}$  of the form

$$\begin{aligned} \lambda u_{m,n} = & \mathcal{A}_{mn}u_{m+1,n} + \mathcal{B}_{mn}u_{m-1,n} + \mathcal{C}_{mn}u_{m,n+1} + \mathcal{D}_{mn}u_{m,n-1} \\ & + \mathcal{E}_{mn}(u_{m+1,n+1} + u_{m-1,n-1} - u_{m+1,n-1} - u_{m-1,n+1}) \\ & + \mathcal{F}_{mn}u_{m,n}, \end{aligned} \quad (26)$$

where  $\mathcal{A}_{mn}, \mathcal{B}_{mn}, \dots, \mathcal{F}_{mn}$  are all functions of  $(m, n)$ . For the grid points at the outermost circle, the boundary condition requires that  $u_{M,n} = 0$  for all  $n$ , and therefore only the  $(M-1) \times N$  difference relations that result from the other  $(M-1) \times N$  grid points need to be considered.

However, extra caution should be taken when applying Eq. (26) to grid points at the innermost circle ( $m=1$ ). Although the origin was excluded from the grid points to avoid infinite values for the coefficients  $\mathcal{A}_{mn}, \mathcal{B}_{mn}, \dots$ , at  $r=0$ , it is inevitable that the value of  $u_{0,n}$  at the origin is needed for the evaluation of Eq. (26) for grid points at the first concentric circle ( $m=1$ ). Fortunately, the value of  $u_0 \equiv u(0, \theta)$  can

be estimated from its neighboring points using the original differential equation, Eq. (15), in Cartesian coordinates, which, in the difference approximation, can be expressed as

$$\begin{aligned} -\lambda u_0 = & \alpha \left. \frac{\partial^2 u}{\partial x^2} \right|_{r=0} + \beta \left. \frac{\partial^2 u}{\partial y^2} \right|_{r=0} \\ \approx & \alpha \frac{[u(\delta r, 0) + u(\delta r, \pi) - 2u_0]}{(\delta r)^2} \\ & + \beta \frac{[u(\delta r, \pi/2) + u(\delta r, 3\pi/2) - 2u_0]}{(\delta r)^2} \end{aligned} \quad (27)$$

at  $r=0$ , and then  $u_0$  is solved as a linear combination of wave-function values  $u_{mn}$  at adjacent points:

$$\begin{aligned} u_0 = & \frac{\alpha(u_{1,0} + u_{1,\theta_n=\pi}) + \beta(u_{1,\theta_n=\pi/2} + u_{1,\theta_n=3\pi/2})}{(\delta r)^2 \lambda + 2(\alpha + \beta)} \\ \approx & \frac{\alpha(u_{1,0} + u_{1,\theta_n=\pi}) + \beta(u_{1,\theta_n=\pi/2} + u_{1,\theta_n=3\pi/2})}{2(\alpha + \beta)} \end{aligned} \quad (28)$$

when

$$(\delta r)^2 \ll \frac{2(\alpha + \beta)}{\lambda}. \quad (29)$$

Thus, we are able to express the  $(M-1) \times N$  difference equations from Eq. (26) in a matrix form:

$$\begin{pmatrix} H_{(1,0)(1,0)} & \cdots & \cdots & H_{(1,0)(M-1,N-1)} \\ \vdots & & & \vdots \\ \vdots & & & \vdots \\ \vdots & & \hat{\mathcal{H}} & \vdots \\ \vdots & & & \vdots \\ \vdots & & & \vdots \\ \vdots & & & \vdots \\ H_{(M-1,N-1)(1,0)} & \cdots & \cdots & H_{(M-1,N-1)(M-1,N-1)} \end{pmatrix} \times \begin{pmatrix} u_{1,0} \\ u_{1,1} \\ \vdots \\ u_{1,N-1} \\ u_{2,0} \\ \vdots \\ \vdots \\ u_{M-1,N-1} \end{pmatrix} = \lambda \begin{pmatrix} u_{1,0} \\ u_{1,1} \\ \vdots \\ u_{1,N-1} \\ u_{2,0} \\ \vdots \\ \vdots \\ u_{M-1,N-1} \end{pmatrix}, \quad (30)$$

where  $\hat{\mathcal{H}}$  is the Hamiltonian matrix established from the coefficients in Eqs. (26) and (28), and the eigenvalues of  $\hat{\mathcal{H}}$  can be evaluated numerically using modern mathematical packages. The number of eigenvalues obtained through this numerical method is equal to  $(M-1) \times N$ . However, higher

TABLE I. Comparisons of the lowest 4 eigenvalues of Eq. (15) derived from analytic solutions and numerical calculations for  $\alpha = \beta$ . These eigenvalues correspond to the subband energy levels of the  $T$ -point holes for trigonal Bi nanowires ( $\alpha = 16.95m_0^{-1}$ ) with an infinite potential height.

Analytic solution $\lambda_A(d_w^2/4\alpha)$	Numerical solution $\lambda_N(d_w^2/4\alpha)$	Degeneracy
5.783	5.784	1
14.6812	14.669	2
26.374	26.262	2
30.4712	30.468	1

eigenvalues usually have larger discrepancies and should be discarded. The criterion for dependable eigenvalues can be determined by

$$\lambda \ll \frac{\alpha + \beta}{(\delta r)^2 + (d_w \delta \theta / 2)^2}. \quad (31)$$

Table I compares the lowest few eigenvalues  $\lambda_A$  and their degeneracies derived from the analytic solutions and  $\lambda_N$  from numerical solutions (with  $M = 64$  and  $N = 40$ ) for the special case  $\alpha = \beta$  where analytic solutions can also be obtained. The numerical solutions  $\lambda_N$  are in excellent agreement with the analytic solutions  $\lambda_A$ , and the relative errors are smaller than 0.5% for all the values listed in Table I. By increasing the number of concentric circles  $M$  and sectors  $N$  simultaneously, even higher accuracy can be obtained. For  $\alpha \neq \beta$ , the numerical technique developed here provides a powerful approach to calculate the eigenvalues accurately and efficiently. In addition, wave functions  $u(\mathbf{r})$  for the eigenstates can be readily derived by solving for the eigenvectors of the Hamiltonian matrix  $\hat{\mathcal{H}}$ .

### C. Nonparabolic band structure in Bi nanowires

In the previous sections, we have developed solutions for the  $T$ -point holes with parabolic dispersion relations. At the  $L$  points, however, the bands are highly nonparabolic due to the strong coupling between the  $L$ -point electrons and holes,<sup>21</sup> and this nonparabolic band structure must be taken into account when determining the subband energy levels and the 1D dispersion relations for the  $L$ -point carriers. The dispersion relation for the  $L$ -point bands is described by the two-band Lax model,<sup>22</sup> which can be written as

$$\frac{\hbar^2}{2} \mathbf{k} \cdot \boldsymbol{\alpha} \cdot \mathbf{k} = E(\mathbf{k}) \left( 1 + \frac{E(\mathbf{k})}{E_{gL}} \right) \quad (32)$$

for the conduction band at the  $L$  point, where  $\boldsymbol{\alpha}$ , is the inverse effective mass tensor at the band edge and  $E_{gL}$  ( $= 15$  meV at 77 K, Ref. 5) is the direct band gap at the  $L$  point. By the effective mass theorem, we obtain a differential equation for the envelope function  $\Psi(\mathbf{r})$  of the  $L$ -point electrons:

$$-\frac{\hbar^2}{2} \nabla \cdot \boldsymbol{\alpha} \cdot \nabla \Psi(\mathbf{r}) = E \left( 1 + \frac{E}{E_{gL}} \right) \Psi(\mathbf{r}). \quad (33)$$

We note that Eq. (33) will have the same form as the Schrödinger equation [Eq. (8)] for parabolic carrier pockets, if we define a *primitive* energy

$$\tilde{E} \equiv E \left( 1 + \frac{E}{E_{gL}} \right), \quad (34)$$

and the same procedures described in Secs. II A and II B can be applied to solve for this *primitive* energy  $\tilde{E}$ :

$$\tilde{E}_{nm}(k_z) = \tilde{\varepsilon}_{nm} + \frac{\hbar^2 k_z^2}{2\tilde{m}_z}, \quad (35)$$

where  $\tilde{\varepsilon}_{nm}$  is the *primitive* subband energy and  $\tilde{m}_z$  is the *primitive* effective mass along the wire axis, in correspondence to Eq. (14). The true quantized subband energy levels and the 1D dispersion relations for each subband can be derived readily by solving  $E$  in Eq. (34) as

$$E_{nm}(k_z) = -\frac{E_{gL}}{2} + \frac{E_{gL}}{2} \sqrt{1 + 4 \frac{\tilde{E}_{nm}(k_z)}{E_{gL}}}, \quad (36)$$

and the band edge energy of each subband is then given by

$$\begin{aligned} \varepsilon_{nm} &\equiv E_{nm}(k_z = 0) \\ &= -\frac{E_{gL}}{2} + \frac{E_{gL}}{2} \sqrt{1 + \frac{4\tilde{\varepsilon}_{nm}}{E_{gL}}} \\ &= (\gamma_{nm} - 1) \frac{E_{gL}}{2}, \end{aligned} \quad (37)$$

where

$$\gamma_{nm} \equiv \sqrt{1 + \frac{4\tilde{\varepsilon}_{nm}}{E_{gL}}}. \quad (38)$$

We note that the 1D dispersion relation  $E_{nm}(k_z)$  in Eq. (36) for each subband is more complicated than Eq. (14) and also is nonparabolic. However, for energies near the subband edge, it is a good approximation to treat the full dispersion relation in Eq. (36) near the subband edge with a Taylor expansion as

$$\begin{aligned} E_{nm}(k_z) &= -\frac{E_{gL}}{2} + \frac{E_{gL}}{2} \sqrt{1 + \frac{4\tilde{\varepsilon}_{nm}}{E_{gL}} + \frac{2\hbar^2 k_z^2}{\tilde{m}_z E_{gL}}} \\ &\simeq \varepsilon_{nm} + \frac{\hbar^2 k_z^2}{2m_{z,nm}^*}, \end{aligned} \quad (39)$$

where

$$m_{z,nm}^* = \sqrt{1 + \frac{4\tilde{\varepsilon}_{nm}}{E_{gL}}} \tilde{m}_z = \gamma_{nm} \tilde{m}_z \quad (40)$$

is the transport effective mass along the wire axis for the corresponding subband. As indicated in Eq. (40), the transport effective masses  $m_{z,nm}^*$  increase with the subband edge energy, and are different for every subband.

It should be noted that in deriving the nonparabolic dispersion relation Eq. (32), the far band contribution ( $\hbar^2 \mathbf{k}^2 / 2m_0$ ) is usually neglected when applying  $\mathbf{k} \cdot \mathbf{p}$  pertur-

TABLE II. Calculated effective mass components of each carrier pocket for determining the band structure in Bi nanowires at 77 K along the indicated crystallographic directions, based on the effective mass parameters of bulk Bi given in Refs. 5 and 6. The  $z'$  direction is chosen along the wire axis. All mass values in this table are in units of the free electron mass,  $m_0$ .

Mass component		Trigonal	Binary	Bisectrix	[01 $\bar{1}$ 2]	[10 $\bar{1}$ 1]
$e^-$ pocket $L(A)$	$m_{x'}$	0.1175	0.0023	0.0023	0.0029	0.0024
	$m_{y'}$	0.0012	0.2659	0.0012	0.0012	0.0012
	$\tilde{m}_{z'}$	0.0052	0.0012	0.2630	0.2094	0.2542
$e^-$ pocket $L(B)$	$m_{x'}$	0.1175	0.0023	0.0023	0.0016	0.0019
	$m_{y'}$	0.0012	0.0016	0.0048	0.0125	0.0071
	$\tilde{m}_{z'}$	0.0052	0.1975	0.0666	0.0352	0.0526
$e^-$ pocket $L(C)$	$m_{x'}$	0.1175	0.0023	0.0023	0.0016	0.0019
	$m_{y'}$	0.0012	0.0016	0.0048	0.0125	0.0071
	$\tilde{m}_{z'}$	0.0052	0.1975	0.0666	0.0352	0.0526
$T$ -point hole pocket	$m_{x'}$	0.0590	0.6340	0.6340	0.1593	0.3261
	$m_{y'}$	0.0590	0.0590	0.0590	0.0590	0.0590
	$m_{z'}$	0.6340	0.0590	0.0590	0.2349	0.1147

bation theory to bulk bismuth, due to the very small effective masses at the 3D band edge for strongly coupled bands. However, for Bi nanowires where the 3D  $L$ -point energy splits into many subbands, the far band contributions are not negligible for higher subbands where the effective masses at the subband edge are not small compared to the free electron mass  $m_0$ . We therefore write the more complete expression to relate  $m_{z,nn}^*$  to  $\tilde{m}_z$ :

$$\frac{1}{m_{z,nn}^*} = \frac{1}{m_0} + \frac{1}{\gamma_{nm}\tilde{m}_z}. \quad (41)$$

#### D. Band shifting and the semimetal-semiconductor transition in Bi nanowires

Based on the band structure parameters of bulk bismuth, values of  $m_{x'}$ ,  $m_{y'}$ , and  $m_{z'}$  (or  $\tilde{m}_z$ ) at 77 K for Bi nanowires oriented along the three principal crystallographic axes (trigonal, binary, and bisectrix directions), and the preferential [01 $\bar{1}$ 2] and [10 $\bar{1}$ 1] growth directions [or (0,0.8339, 0.5519) and (0,0.9503,0.3112), respectively, in Cartesian coordinates defined by the binary ( $x$ ), the bisectrix ( $y$ ), and the trigonal ( $z$ ) axes] are given in Table II. In Table II and for the following discussions, the three  $L$ -point electron pockets in Bi are denoted by  $L_e(A)$ ,  $L_e(B)$ , and  $L_e(C)$ . The  $L_e(A)$  pocket is chosen as the one with its major axis lying close to a bisectrix axis, and the pockets  $L_e(B)$  and  $L_e(C)$  are obtained by rotating the pocket  $L_e(A)$  by  $120^\circ$  and  $-120^\circ$  about the trigonal axis, respectively. For the  $L$ -point pockets, Eqs. (40) and (41) should be used to include nonparabolic effects into the entries in Table II, while the parabolic approximation of Eq. (39) was used to describe the small energy excursions from  $k_{z'}=0$  for the dispersion along the wire axis.

Since Bi nanowires with smaller wire diameters ( $<40$  nm) tend to be oriented along the [01 $\bar{1}$ 2] direction, the calculated lowest subband energies for Bi quantum wires oriented along this preferred growth direction at 77 K are shown in Fig. 2 as a function of wire diameter. For the

[01 $\bar{1}$ 2] wires, the degeneracy at the  $L$  points is lifted, resulting in two inequivalent groups of carrier pockets: a single electron pocket  $L_e(A)$  and two electron pockets  $L_e(B,C)$  with the same symmetry and band parameters as each other, but different from those for the  $L_e(A)$  pocket. Since the  $L_e(A)$  pocket has smaller mass components ( $m_{x'}$ ,  $m_{y'}$ ) in the quantum confined directions than the electron pockets  $L_e(B,C)$  (see Table II), the  $L_e(A)$  pocket forms a higher conduction subband, while the pockets  $L_e(B,C)$  form a two-fold degenerate subband at a lower energy (see Fig. 2). Because of the larger mass component along the wire axis ( $m_{z'}$ ) for the electron pocket  $L_e(A)$  than for  $L_e(B,C)$ , the dispersion relation of the  $L_e(A)$  subband has a smaller curvature (see Fig. 2). The band edge of the lowest subband of

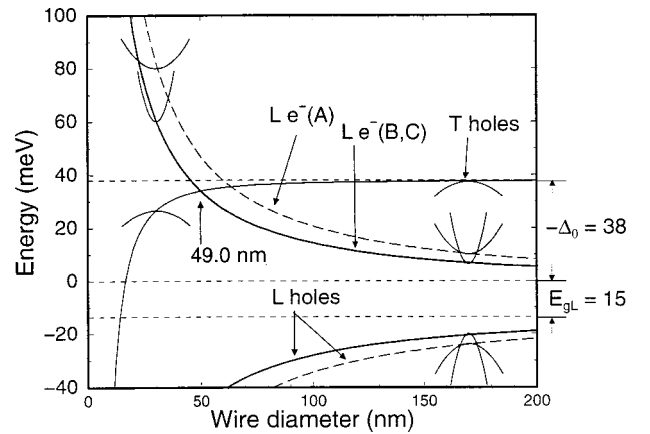


FIG. 2. The subband structure at 77 K of Bi quantum wires oriented along the [01 $\bar{1}$ 2] growth direction, showing the energies vs wire diameter of the highest subbands for the  $T$ -point hole carrier pocket as well as for the  $L$ -point holes, and the lowest subbands for the  $L$ -point electron pockets ( $A$ ,  $B$  and  $C$ ). The zero energy refers to the conduction band edge in bulk Bi. As  $d_w$  decreases, the conduction subbands move up in energy, while the valence subbands move down. At  $d_c=49.0$  nm, the lowest conduction subband edge formed by the  $L(B,C)$  electrons crosses the highest  $T$ -point valence subband edge, and a semimetal-semiconductor transition occurs.

TABLE III. Calculated critical wire diameters  $d_c$  for Bi nanowires oriented along various crystallographic directions at 77 K. The predicted values of the critical wire diameters and the critical wire widths from the cyclotron effective mass approximation and the square wire approximation, respectively, are also included for comparison. The values in the table are given in units of nm.

Calculation method	Trigonal	Binary	Bisectrix	$[10\bar{1}1]$	$[01\bar{1}2]$
Circular wire + numerical	55.1	39.8	48.5	48.7	49.0
Square wire approx. <sup>a</sup>	52.1	34.5	41.3	NA	NA
Cyclotron effective mass approx. <sup>b</sup>	33	20	44	45	NA

<sup>a</sup>Reference 24.

<sup>b</sup>Reference 12.

the  $L_e(B, C)$  electrons increases with decreasing wire diameter  $d_w$ , while the highest subband edges of the  $T$ -point and  $L$ -point holes move downwards in energy. For  $d_w < 49.0$  nm, the energy of the lowest  $L$ -point conduction subband edge exceeds that of the highest  $T$ -point valence subband edge, indicating that these nanowires have become semiconducting.

In addition to the wire diameter, the subband structure of the 1D Bi quantum wires is also strongly dependent on the wire orientation. The bisectrix wires and the  $[10\bar{1}1]$  wires have the same symmetry as the  $[01\bar{1}2]$  wires, and, therefore, the three wire orientations (bisectrix,  $[10\bar{1}1]$ , and  $[01\bar{1}2]$ ) possess similar subband structures (see Fig. 2) with slightly different critical wire diameters for the semimetal-semiconductor (SM-SC) transition. For the trigonal wires, the subband energies of the three  $L$ -point electron pockets remain degenerate for all wire diameters, and the critical wire diameter for the SM-SC transition at 77 K occurs at  $d_c = 55.1$  nm. For binary wires, the electron pockets  $L_e(B, C)$  form a twofold degenerate subband at a higher energy than the electron pocket  $L_e(A)$  in contrast to Fig. 2. A more detailed study of the band structure of Bi nanowires for these wire orientations is given in Ref. 23.

The calculated critical wire diameters  $d_c$  for the SMSC transition for Bi nanowires oriented along the three principal crystallographic axes, the  $[01\bar{1}2]$ , and the  $[10\bar{1}1]$  directions at 77 K are listed in Table III, in which the critical wire width  $a_c$  predicted by the square wire approximation<sup>24</sup> and the critical wire diameter  $d_c$  obtained by the cyclotron effective mass approximation<sup>12</sup> for available directions are also included for comparison.

It should be noted that since  $d_c$  is determined by the band structure of crystalline Bi, which is strongly temperature dependent for  $T > 80$  K,<sup>25,26</sup> the critical wire diameter  $d_c$  for the SM-SC transition will also be  $T$  dependent at high temperatures ( $T > 80$  K). The  $T$  dependence of  $d_c$  has been calculated using the best available values for the temperature dependence of the bismuth band parameters, which are given in Table IV. Figure 3 shows the resulting calculated critical wire diameter  $d_c$  for the SM-SC transition in Bi nanowires as a function of temperature for different wire orientations. Since the overlap energy  $\Delta_0$  between the  $L$ -point conduction band and the  $T$ -point valence band and the effective mass components of the  $L$ -point electrons both increase with temperature (see Table IV), a smaller wire diameter is required to achieve the transition at higher temperatures. At 300 K, the critical wire diameters where the SM-SC transition occurs are estimated as 15.4, 11.2, 13.6, 14.0, and 13.6 nm for nanowires oriented along the trigonal, binary, bisectrix,  $[01\bar{1}2]$ , and  $[10\bar{1}1]$  crystallographic directions, respectively.

Based on the band structure derived for 1D Bi quantum wires, the carrier concentration for undoped Bi nanowires has been calculated by adjusting the Fermi level so that the number of holes is equal to the number of electrons. Figure 4 shows the calculated total carrier densities of Bi nanowires oriented along the  $[01\bar{1}2]$  growth direction as a function of temperature for different wire diameters. Since the critical wire diameter  $d_c$  is temperature dependent, three different types of temperature dependences of the carrier densities are predicted for Bi nanowires, depending on the wire diameters. For 10 nm Bi nanowires, which are always in the semicon-

TABLE IV. Temperature dependence of selected bulk Bi band structure parameters.

Parameters	Temperature Dependence
Band overlap (meV) <sup>a</sup>	$\Delta_0 = \begin{cases} -38 & (T < 80 \text{ K}) \\ -38 - 0.044(T - 80) + 4.58 \times 10^{-4}(T - 80)^2 - 7.39 \times 10^{-6}(T - 80)^3 & (T > 80 \text{ K}) \end{cases}$
$L$ -point direct band gap (meV) <sup>b</sup>	$E_{gL} = 13.6 + 2.1 \times 10^{-3}T + 2.5 \times 10^{-4}T^2$
$L$ -point electron	$[\mathbf{m}_e(T)]_{ij} = \frac{[\mathbf{m}_e(0)]_{ij}}{1 - 2.94 \times 10^{-3}T + 5.56 \times 10^{-7}T^2}$
Effective mass components <sup>b,c,d</sup>	

<sup>a</sup>Reference 25.

<sup>b</sup>Reference 26.

<sup>c</sup>Reference 6.

<sup>d</sup> $\mathbf{m}_e(0)$  is the effective mass tensor at  $T = 0$  K.

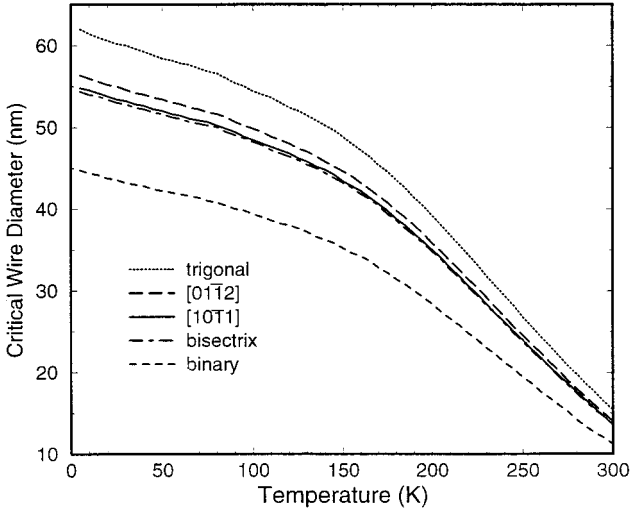


FIG. 3. Calculated critical wire diameter  $d_c$  for the semimetal-semiconductor transition as a function of temperature for Bi nanowires oriented along different directions.

ductor regime up to 300 K (see Fig. 3), the carrier density increases exponentially with  $T$  up to 300 K. On the other hand, for 80 nm Bi nanowires, which remain in the semimetallic regime even down to 0 K, the carrier density has a similar temperature dependence to that of bulk Bi. The smaller carrier density of the 80 nm nanowires compared to bulk Bi arises because of the smaller overlap between the conduction and the valence bands in Bi nanowires as compared to bulk Bi. As for the 40 nm Bi nanowires, the temperature for the SM-SC transition is predicted to be around 170 K for a  $[01\bar{1}2]$  nanowire (see Fig. 3). Thus, for  $T \leq 170$  K, 40 nm Bi nanowires are in the semiconductor regime, and the carrier density drops significantly with decreasing temperature, while for  $T > 170$  K, the nanowires are in the semimetal regime, and the carrier density has a similar temperature dependence to that of bulk Bi. It should also be noted that for semiconducting wires, the slope of the curves in Fig. 4 is approximately proportional to the band gap be-

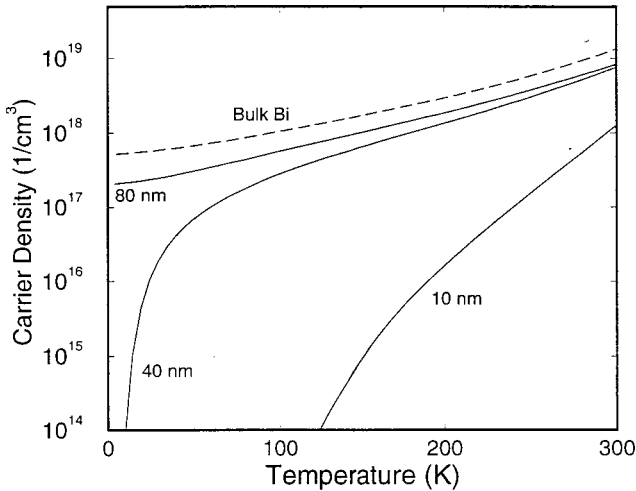


FIG. 4. Calculated total carrier density (electrons and holes) of Bi nanowires oriented along the  $[01\bar{1}2]$  direction as a function of temperature for different wire diameters: 10 nm, 40 nm, and 80 nm, in comparison to that for bulk Bi.

tween the conduction band and the valence band, while the semiconducting band gap increases with decreasing  $T$  for 40 nm Bi nanowires below 170 K. Therefore, the slope of the curve for 40 nm Bi nanowires in Fig. 4 decreases with increasing  $T$ .

### III. THEORETICAL MODELING FOR THERMOELECTRIC TRANSPORT PROPERTIES

#### A. Semiclassical transport model for Bi nanowires

The thermoelectric related transport coefficients of Bi nanowires can be obtained from a semiclassical model, which is based on the Boltzmann transport equation. For a one-band system in a 1D quantum wire, important thermoelectric-related transport coefficients such as the electrical conductivity  $\sigma$ , the Seebeck coefficient  $S$ , and the thermal conductivity  $\kappa_e$  are derived as<sup>13,27</sup>

$$\sigma = \mathcal{L}^{(0)}, \quad (42)$$

$$S = -\frac{1}{eT} \frac{\mathcal{L}^{(1)}}{\mathcal{L}^{(0)}}, \quad (43)$$

$$\kappa_e = \frac{1}{e^2 T} \left( \mathcal{L}^{(2)} - \frac{(\mathcal{L}^{(1)})^2}{\mathcal{L}^{(0)}} \right), \quad (44)$$

where  $T$  is the temperature and

$$\mathcal{L}^{(\alpha)} = e^2 \int \frac{4dk}{\pi^2 d^2} \left( -\frac{df}{dE} \right) \tau(k) v(k) v(k) [E(k) - E_F]^\alpha, \quad (45)$$

in which  $\alpha=0,1,2$ ,  $E(k)$  is the carrier dispersion relation,  $\tau(k)$  is the relaxation time,  $E_F$  is the Fermi energy, and  $f(E)$  is the Fermi-Dirac distribution function. For a one-band system with a parabolic dispersion relation, the transport elements  $\mathcal{L}^{(\alpha)}$  in Eqs. (42)–(44) are derived as

$$\mathcal{L}^{(0)} = D \left[ \frac{1}{2} F_{-1/2} \right], \quad (46)$$

$$\mathcal{L}^{(1)} = \begin{cases} (k_B T) D \left[ \frac{3}{2} F_{\frac{1}{2}}^1 - \frac{1}{2} \zeta^* F_{-1/2} \right] & \text{(for electrons)} \\ -(k_B T) D \left[ \frac{3}{2} F_{\frac{1}{2}}^1 - \frac{1}{2} \zeta^* F_{-1/2} \right] & \text{(for holes),} \end{cases} \quad (47)$$

$$\mathcal{L}^{(2)} = (k_B T)^2 D \left[ \frac{5}{2} F_{3/2} - 3 \zeta^* F_{1/2} + \frac{1}{2} \zeta^{*2} F_{-1/2} \right], \quad (48)$$

where  $D$  is given by

$$D = \frac{8e}{\pi^2 d_w^2} \left( \frac{2m^* k_B T}{\hbar^2} \right)^{1/2} \mu, \quad (49)$$

in which  $\mu$  is the carrier mobility along the nanowire and

$$F_j = \int_0^\infty \frac{x^j dx}{e^{(x-\zeta^*)} + 1} \quad (50)$$

denotes the Fermi-Dirac related functions, with fractional indices  $j = -\frac{1}{2}, \frac{1}{2}, \frac{3}{2}, \dots$ . The reduced chemical potential  $\zeta^*$  is defined as

$$\zeta^* = \begin{cases} (E_F - \varepsilon_e^{(0)})/k_B T & \text{(for electrons),} \\ (\varepsilon_h^{(0)} - E_F)/k_B T & \text{(for holes),} \end{cases} \quad (51)$$

where  $\varepsilon_e^{(0)}$  and  $\varepsilon_h^{(0)}$  denotes the band edges for electrons and holes, respectively.

For the Bi quantum wire system, there are many 1D subbands due to the multiple carrier pockets at the  $L$  points and the  $T$  point, and the quantum confinement-induced band splitting also forms a set of 1D subbands from a single band in the bulk material. Therefore, when considering the transport properties of real 1D nanowire systems, contributions from all of the subbands near the Fermi energy should be included, and the  $\mathcal{L}^{(\alpha)}$ 's in Eqs. (42)–(44) should be replaced by the sum  $\mathcal{L}_{\text{total}}^{(\alpha)} = \sum_i \mathcal{L}_i^{(\alpha)}$  of contributions from each subband (labeled by  $i$ ) to obtain the various transport coefficients.

Another physical quantity of interest in thermoelectric applications for Bi quantum wire systems is the lattice thermal conductivity  $\kappa_L$ , which, together with the electronic thermal conductivity  $\kappa_e$ , determines the total thermal conductivity of the system. The lattice thermal conductivity in the 1D systems has been studied by using the Boltzmann equation for phonons and considering the diffusive and specular phonon scattering at the wire boundary.<sup>28</sup> The calculated results showed that  $\kappa_L$  decreases significantly below the bulk value for small diameters. In this study, we use a simpler approach to estimate  $\kappa_L$  for Bi nanowire systems as follows. From the kinetic theory, the thermal conductivity of phonons is given by<sup>29</sup>

$$\kappa_L = \frac{1}{3} C_v v l, \quad (52)$$

where  $C_v$  is the heat capacity per unit volume,  $v$  is the sound velocity, and  $l$  is the mean free path for phonons. We note that the wide band-gap host material that confines electrons cannot confine the phonon paths, and thus, because of acoustic mismatch, phonons will be scattered when they move across the wire boundary. Therefore, if the phonon mean free path  $l_B$  in bulk Bi is greater than the wire diameter  $d_w$ , then  $l$  and  $\kappa_L$  are mainly limited by the predominant phonon scattering at the wire boundary, and the lattice thermal conductivity of the quantum wire system is obtained approximately<sup>3,30</sup> by setting  $l = d_w$  and using Eq. (52). On the other hand, the bulk value of  $\kappa_L$  is used for a conservative estimation of the thermal conductivity of Bi nanowire systems if  $d_w$  is larger than  $l_B$ .

### B. Calculation of $Z_{1D}T$ of Bi nanowires at 77 K

The efficiency of a thermoelectric material is measured by the dimensionless figure of merit<sup>31</sup>

$$ZT = \frac{S^2 \sigma T}{\kappa}, \quad (53)$$

TABLE V. Calculated mobility along the wire for each carrier pocket in Bi nanowires with various wire orientations at 77 K, based on experimental values of bulk Bi in Ref. 33. The values are given in  $\text{m}^2 \text{V}^{-1} \text{s}^{-1}$ .

Mobility	Trigonal	Binary	Bisectrix	[10 $\bar{1}$ 1]	[01 $\bar{1}$ 2]
$e^-$ pocket A	25.93	68.11	1.08	1.10	1.32
$e^-$ pocket B	25.93	1.42	4.11	5.21	7.59
$e^-$ pocket C	25.93	1.42	4.11	5.21	7.59
Hole pocket	2.10	11.84	11.84	8.17	4.91

where  $\kappa = \kappa_e + \kappa_L$  is the total thermal conductivity due to both electron and phonons. In the following, we calculate the  $Z_{1D}T$  for Bi nanowires at 77 K by using the general formalism derived in Sec. III A.

Since the mobility tensors for electrons and holes are anisotropic, the mobility  $\mu_i$  for carriers traveling along the wire axis depends on the wire orientation, and  $\mu_i$  is given by

$$\mu_i = (\hat{\mathbf{I}} \cdot \boldsymbol{\mu}^{-1} \cdot \hat{\mathbf{I}})^{-1} \quad (54)$$

where  $\hat{\mathbf{I}}$  is the unit vector along the wire axis. Equation (54) follows from the general definition of the carrier mobility in terms of  $\boldsymbol{\mu} = e \tau / m^*$  and from Matthiessen's rule summing  $1/\tau_i$  for each scattering process  $i$ .<sup>32</sup> Table V lists the mobilities along the wire calculated using Eq. (54) for each carrier pocket in Bi nanowires at 77 K for various wire orientations.<sup>33</sup>

The lattice thermal conductivity in bulk Bi is also anisotropic, and  $\kappa_{L,i}$  along the wire axis is given by

$$\kappa_{L,i} = \hat{\mathbf{I}} \cdot \boldsymbol{\kappa}_L \cdot \hat{\mathbf{I}} = \cos^2 \theta \kappa_{L,\perp} + \sin^2 \theta \kappa_{L,\parallel}, \quad (55)$$

where  $\kappa_{L,\parallel}$  and  $\kappa_{L,\perp}$  are the thermal conductivities parallel and perpendicular to the trigonal axis, respectively, and  $\theta$  is the angle between the wire axis and the trigonal axis. The measured values of  $\kappa_{L,\perp}$  and  $\kappa_{L,\parallel}$  of bulk Bi at 77 K are 13.2 and 9.9 W/mK,<sup>25</sup> respectively. For Bi at 77 K, the heat capacity  $C_v \approx 1.003 \text{ J K}^{-1} \text{ cm}^{-3}$ ,<sup>34</sup> and the estimated sound velocities  $v$  along the selected directions are listed in Table VI, which are extrapolated from measured values.<sup>35,36</sup>

Using the general formalism presented in Sec. III A for  $S$ ,  $\sigma$ ,  $\kappa_e$ , and  $\kappa_{L,i}$  and the above discussion to account for the multiple carrier pockets and their anisotropy, the thermoelectric figure of merit  $Z_{1D}T$  has been calculated. Figure 5 shows the calculated  $Z_{1D}T$  for  $n$ -type Bi nanowires oriented along the trigonal axis at 77 K as a function of donor concentration  $N_d$  for three different diameters. We note that the value of  $Z_{1D}T$  for a given  $N_d$  increases drastically with decreasing wire diameter  $d_w$ , and the maximum  $Z_{1D}T$  for each diameter occurs at an optimized donor concentration  $N_{d(\text{opt})}$ , which

TABLE VI. The sound velocities  $v$  (in  $10^5$  cm/s) of Bi at 77 K along the three principal axes and other selected directions. The values are interpolated from the measured results at 1.6 K (Ref. 35) and 300 K (Ref. 36).

Orientation	Trigonal	Binary	Bisectrix	[10 $\bar{1}$ 1]	[01 $\bar{1}$ 2]
$v$ ( $10^5$ cm/s)	2.01	2.60	2.67	2.45	2.24

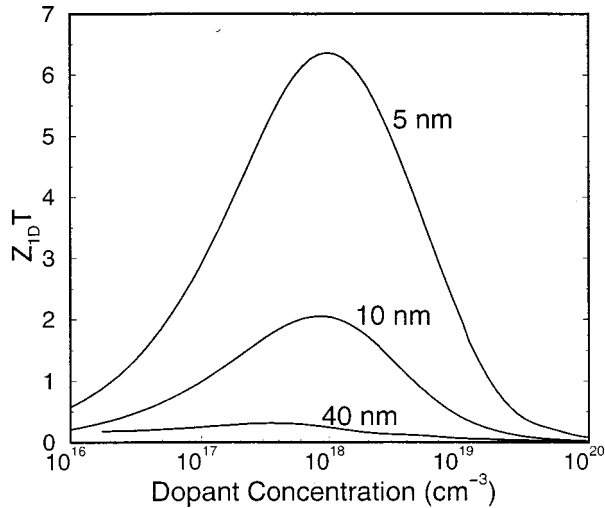


FIG. 5. Calculated  $Z_{1D}T$  for  $n$ -type Bi nanowires oriented along the trigonal axis at 77 K as a function of donor concentration for three different wire diameters.

increases somewhat as  $d_w$  decreases. For 5 nm Bi nanowires oriented along the trigonal axis at 77 K, the maximum calculated  $Z_{1D}T$  is about 6 with an optimized  $N_{d(\text{opt})} \approx 10^{18} \text{ cm}^{-3}$ . The value of  $Z_{1D}T$  also strongly depends on the wire orientation due to the anisotropic nature of the Bi band structure and of the thermal properties. Figure 6 shows the calculated  $Z_{1D}T$  at 77 K as a function of  $N_d$  for 10 nm Bi nanowires oriented in different directions. For 10 nm Bi nanowires at 77 K, the trigonal nanowires have the highest optimal  $Z_{1D}T$ , which is about 2.0, while bisectrix wires have the lowest optimal  $Z_{1D}T \approx 0.4$ . This optimal  $Z_{1D}T$  increases as the wire orientation is varied from the bisectrix axis closer to the trigonal axis, as shown for  $[10\bar{1}1]$  and  $[01\bar{1}2]$  nanowires (see Fig. 6) which, respectively, make an angle of  $71.9^\circ$  and  $56.5^\circ$  with respect to the trigonal axis. The optimum carrier concentrations  $N_{d(\text{opt})}$  and the corresponding  $Z_{1D}T$  of  $n$ -type Bi nanowires at 77 K are listed in Table VII for various wire diameters and orientations. Figure 7 shows the calculated optimal  $Z_{1D}T$  at 77 K as a function of  $d_w$  for  $n$ -type Bi

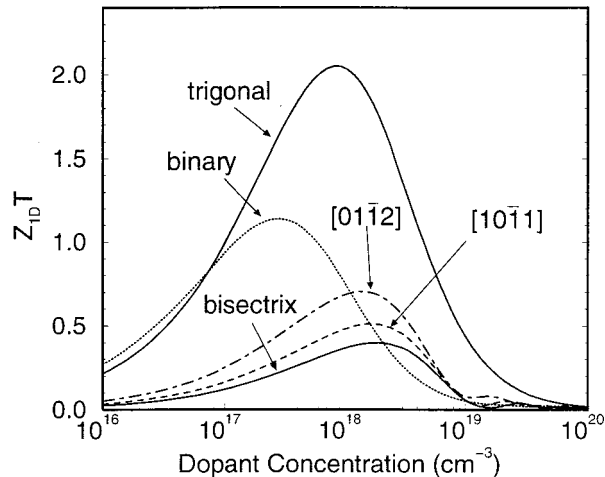


FIG. 6. Calculated  $Z_{1D}T$  at 77 K as a function of donor concentration  $N_d$  for 10 nm  $n$ -type Bi nanowires oriented in different directions: trigonal, binary bisectrix,  $[10\bar{1}1]$ , and  $[01\bar{1}2]$ .

TABLE VII. The optimum carrier concentrations  $N_{d(\text{opt})}$  (in  $10^{18} \text{ cm}^{-3}$ ) and the corresponding  $Z_{1D}T$  of  $n$ -type Bi nanowires calculated at 77 K for various wire diameters and orientations.

Wire Orientation	5 nm		10 nm		40 nm	
	$N_{d(\text{opt})}$	$Z_{1D}T$	$N_{d(\text{opt})}$	$Z_{1D}T$	$N_{d(\text{opt})}$	$Z_{1D}T$
Trigonal	0.96	6.36	0.81	2.0	0.38	0.31
Binary	0.35	3.68	0.28	1.14	0.56	0.13
Bisectrix	4.1	2.21	1.78	0.40	4.97	0.03
$[10\bar{1}1]$	3.21	2.69	1.57	0.51	2.57	0.04
$[01\bar{1}2]$	2.07	3.41	1.33	0.70	2.73	0.06

nanowires with various orientations, which shows a rapid increase in  $Z_{1D}T$  with decreasing  $d_w$ .

Although binary wires have a smaller critical wire diameter  $d_c$  for the SMSC transition than bisectrix wires (see Fig. 3), they have a higher optimal  $Z_{1D}T$  than bisectrix wires at the same wire diameter (see Fig. 7). The dependence of the optimal  $Z_{1D}T$  on the wire orientation can be qualitatively explained by a simple argument considering the dependence of  $Z_{1D}T$  on the effective mass in a 1D system. First, we note that the optimal Fermi energy for the maximum  $Z_{1D}T$  is usually below but very close to the lowest conduction subband edge.<sup>13</sup> Therefore, for semiconducting Bi nanowires with Fermi energies  $E_F$  close to the optimal Fermi level, the system can be approximately described by a one-band model at low temperatures, in which the thermal energy  $k_B T$  is much smaller than the band gap and adjacent subband separations. Since the Seebeck coefficient in a one-band system is fairly independent of the band structure and is determined by the position of  $E_F$  only, the dependence of  $Z_{1D}T$  on the carrier effective mass is only influenced by the electrical conductivity  $\sigma$  and the electronic contribution to the thermal conductivity  $\kappa_e$ . At this Fermi energy range,  $\kappa_e$  is usually small due to the low carrier densities, and the total thermal conductivity is dominated by the lattice thermal conductivity. For a 1D system, the carrier density  $n$  is proportional to  $\sqrt{m^*}$  and to the degeneracy factor  $g$  of the lowest subband, so that the conductivity, which can be written as  $\sigma = ne^2 \tau / m^*$  in a one-band system, will be proportional to

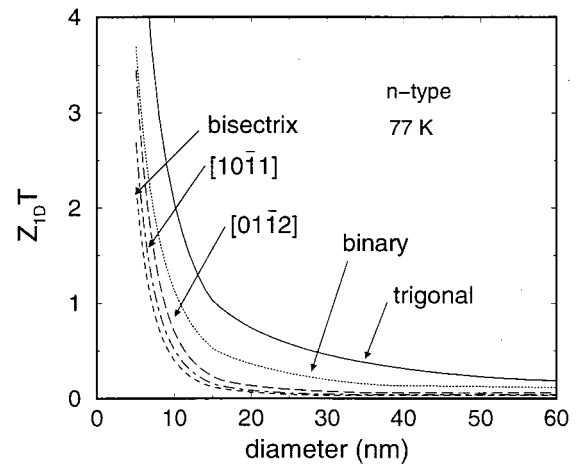


FIG. 7. Calculated  $Z_{1D}T$  at 77 K as a function of  $d_w$  for  $n$ -type Bi nanowires oriented along different directions.

TABLE VIII. The optimum carrier concentrations  $N_{a(\text{opt})}$  (in  $10^{18} \text{ cm}^{-3}$ ) and the corresponding  $Z_{1D}T$  of  $p$ -type Bi nanowires calculated at 77 K for various wire diameters and crystalline orientations.

Wire Orientation	5 nm		10 nm		40 nm	
	$N_{a(\text{opt})}$	$Z_{1D}T$	$N_{a(\text{opt})}$	$Z_{1D}T$	$N_{a(\text{opt})}$	$Z_{1D}T$
Trigonal	0.96	6.36	12.9	0.72	6.2	0.17
Binary	0.79	1.78	10.3	0.16	7.9	0.05
Bisectrix	0.74	0.32	0.19	0.40	0.50	0.07
[10 $\bar{1}$ 1]	1.04	1.16	0.43	0.19	0.63	0.05
[01 $\bar{1}$ 2]	2.59	2.46	0.58	0.18	0.75	0.03

( $gm^*^{-1/2}$ ). Therefore, the optimal  $Z_{1D}T$  is roughly proportional to  $\epsilon \equiv (gm^*^{-1/2})$  in a 1D transport system. The relative values of  $\epsilon$  for Bi nanowires oriented along the trigonal, binary, and bisectrix directions are calculated to be 1:0.69:0.19, respectively, which agrees quite well with the relative values of the calculated optimal  $Z_{1D}T$  of 1:0.57:0.2 for 10 nm Bi nanowires in these three directions (see Table VII). It should be noted that, due to the transport effective mass approximation Eq. (6), instead of Eq. (4) or (12), which was used in the square wire approximation, the previous calculation by Sun *et al.* gave rise to a higher  $Z_{1D}T$  for bisectrix Bi nanowires than for binary wires.<sup>15,24</sup>

For a comparison, the optimum acceptor concentration  $N_{a(\text{opt})}$  and the corresponding  $Z_{1D}T$  for  $p$ -type Bi nanowires are calculated and listed in Table VIII for various wire di-

ameters and orientations. Compared with the results in Table VII for  $n$ -type Bi nanowires, we note that  $p$ -type Bi nanowires of the same  $d_w$ , in general, have a much lower  $Z_{1D}T$ . The asymmetric behavior between  $n$ -type and  $p$ -type Bi nanowires is discussed in the following section.

### C. Effect of $T$ -point holes on the thermoelectric properties of Bi nanowires

In Bi nanowires, due to the presence of  $T$ -point holes that dominate the transport phenomena for  $p$ -type Bi nanowires in most situations, the transport properties exhibit an asymmetric behavior for  $n$ -type and  $p$ -type nanowires. The  $T$ -point holes, which are also anisotropic, have a larger 3D effective mass component ( $\sim 0.634m_0$ ) along the trigonal direction, and smaller effective mass components ( $\sim 0.059m_0$ ) for the binary and the bisectrix directions.<sup>5</sup> The different anisotropy of the  $T$ -point holes relative to the  $L$ -point carriers further complicates the dependence of the thermoelectric properties on the wire orientation.

To reveal the effect of the  $T$ -point holes on the thermoelectric properties of Bi nanowires, we first present  $Z_{1D}T$  results for trigonal Bi wires, in which the three electron pockets at the  $L$  points become degenerate. The solid curves in Fig. 8 show the calculated  $Z_{1D}T$  at 77 K as a function of  $E_F$  for 40 nm, 20 nm, 10 nm, and 5 nm trigonal Bi nanowires, where the zero of energy refers to the  $L$ -point conduction band edge of bulk Bi. The highest subband edges of the  $T$ -point holes and of the  $L$ -point holes are denoted by  $\epsilon_{h(T)}^{(0)}$  and  $\epsilon_{h(L)}^{(0)}$ , respectively, and the lowest subband edge of the

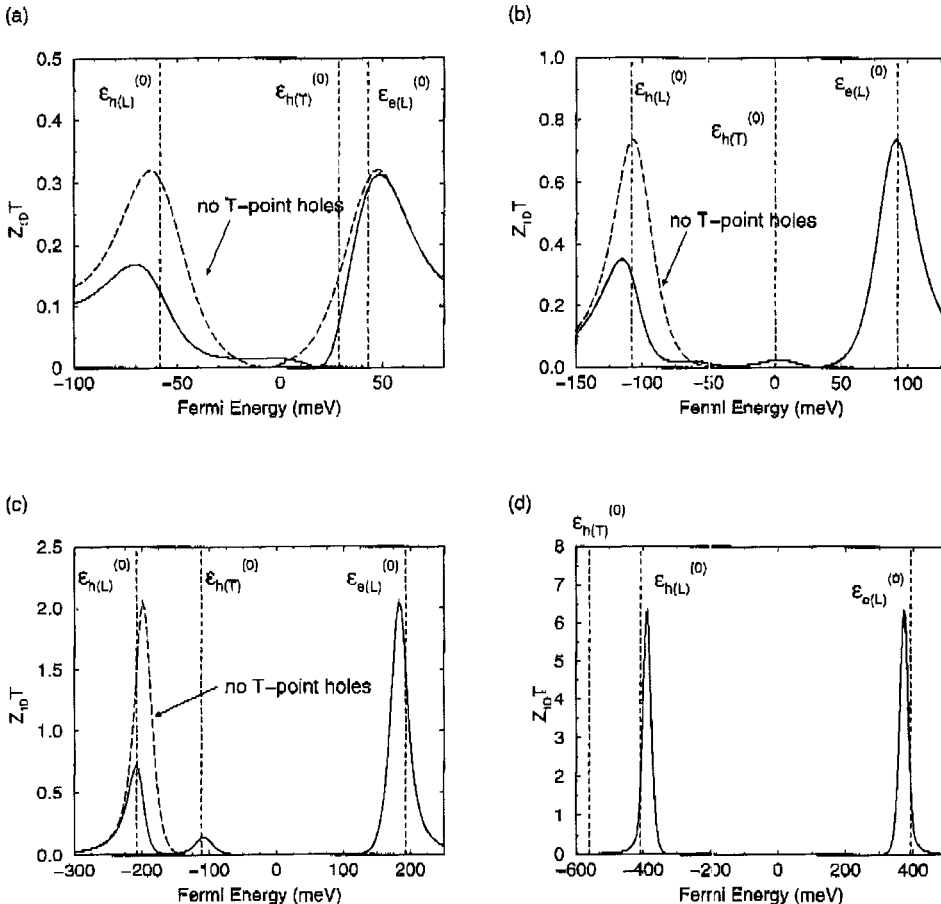


FIG. 8. Calculated  $Z_{1D}T$  as a function of the chemical potential (or Fermi energy) at 77 K for (a) 40 nm, (b) 20 nm, (c) 10 nm, and (d) 5 nm Bi nanowires oriented along the trigonal direction. The zero in energy refers to the conduction band edge in bulk Bi.  $\epsilon_{h(T)}^{(0)}$  and  $\epsilon_{h(L)}^{(0)}$  denote the highest subband edge of the  $T$ -point holes and  $L$ -point holes, respectively, and the lowest subband edge of the  $L$ -point electrons is labeled as  $\epsilon_{e(L)}^{(0)}$ . The solid curves are the  $Z_{1D}T$  calculated with both the  $T$ -point holes and  $L$ -point holes present, and the dashed curves show the  $Z_{1D}T$  when there are no  $T$ -point holes. For 5 nm Bi nanowires, the solid and dashed curves coincide with each other, indicating that the  $T$ -point holes have a negligible effect on the transport properties.

$L$ -point electrons is labeled by  $\varepsilon_{e(L)}^{(0)}$ . The calculated  $Z_{1D}T$  curves usually have two or more extremal values: the extremal  $Z_{1D}T$  with a higher  $E_F$  corresponds to optimal  $n$ -type nanowires, while the extremal  $Z_{1D}T$  with a lower  $E_F$  belongs to optimal  $p$ -type nanowires. The curves for 40 nm to 10 nm nanowires show an asymmetric behavior for the  $p$ -type wires compared to  $n$ -type wires as expected [see Figs. 8(a)–(c)], although 5 nm Bi nanowires exhibit a symmetric behavior for  $n$ -type and  $p$ -type nanowires [see Fig. 8(d)], as discussed below. The calculated  $Z_{1D}T$ , assuming that there were no  $T$ -point holes for the corresponding Bi nanowires, is also sketched in Fig. 8 by the dashed curves, showing a symmetry in  $Z_{1D}T$  for the  $n$ -type and  $p$ -type counterparts due to the symmetric band structures of the  $L$ -point electrons and the  $L$ -point holes.

For 40 nm trigonal nanowires at 77 K,  $\varepsilon_{h(T)}^{(0)}$  is only about 15 meV below  $\varepsilon_{e(L)}^{(0)}$ . The optimized Fermi energy for 40 nm  $n$ -type nanowires is located within the conduction band, and is not far from the valence band edge  $\varepsilon_{h(T)}^{(0)}$ , compared to the 77 K thermal energy  $k_B T$  ( $\sim 6$  meV). Therefore, the presence of the  $T$ -point holes partly cancels the contribution of the electrons to the thermopower  $S$  and the optimal  $Z_{1D}T$  is slightly reduced with respect to the dashed curve [see Fig. 8(a)]. We also note that although both the  $Z_{1D}T$  of the dashed and solid curves decrease as  $E_F$  decreases from the optimized value, the solid curve decays faster due to the increasing influence of the  $T$ -point holes. The adverse influence of the  $T$ -point holes on  $Z_{1D}T$  for  $n$ -type Bi nanowires becomes less significant as  $d_w$  decreases, so that the  $T$ -point valence band is pushed further away from the conduction band. As shown in Figs. 8(b)–(d), the  $T$ -point holes have essentially no effect on  $Z_{1D}T$  for 5 nm to 20 nm  $n$ -type Bi nanowires.

The  $T$ -point holes play a more important role in determining the behavior of  $Z_{1D}T$  of  $p$ -type Bi nanowires than for their  $n$ -type counterparts. For Bi nanowires with diameters of 40 nm to 10 nm, the  $T$ -point holes and the  $L$ -point holes, respectively, mainly contribute to the two  $Z_{1D}T$  extrema [see the solid curves in Figs. 8(a)–(c)] near the subband edges  $\varepsilon_{h(T)}^{(0)}$  and  $\varepsilon_{h(L)}^{(0)}$ . For trigonal nanowires, the  $T$ -point holes have a large effective mass component along the transport direction, and therefore the  $T$ -point holes by themselves will give rise to a small value of  $Z_{1D}T$  and thus are undesirable for  $p$ -type thermoelectric applications. For example, for 10 nm Bi nanowires shown in Fig. 8(c), the  $Z_{1D}T$  variation with  $E_F \approx \varepsilon_{h(T)}^{(0)}$  arises essentially from the  $T$ -point holes only, and the value of this  $Z_{1D}T$  extremum is merely  $\sim 0.14$ , which is much smaller than the optimal value of  $\sim 2$  for  $n$ -type trigonal wires. In addition, even though the  $L$ -point holes are favorable for  $p$ -type thermoelectric materials, just like the  $L$ -point electrons, the presence of heavy-mass  $T$ -point holes reduces the overall thermoelectric performance significantly. As shown in Figs. 8(a)–(c), the values of the optimal  $Z_{1D}T$  with  $E_F \approx \varepsilon_{h(L)}^{(0)}$  are only about 0.17, 0.35, and 0.7 for 40 nm, 20 nm, and 10 nm  $p$ -type nanowires, respectively, which would otherwise be  $\sim 0.32$ , 0.74, and 2.0 if there were no  $T$ -point holes.

For 5 nm Bi nanowires, however, the thermoelectric performance is essentially independent of the presence of  $T$ -point holes, as shown in Fig. 8(d) where the solid curve

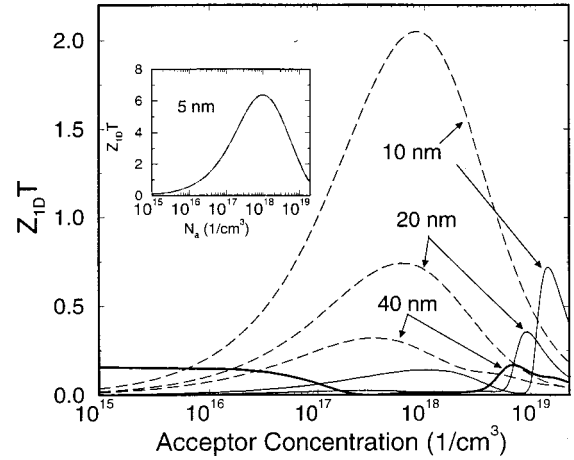


FIG. 9. Calculated  $Z_{1D}T$  for  $p$ -type Bi nanowires of different diameters oriented along the trigonal axis at 77 K as a function of acceptor dopant concentration  $N_a$ . The dashed curves represent the results assuming there are no  $T$ -point holes. The inset shows  $Z_{1D}T$  calculated as a function of  $N_a$  for 5 nm nanowires.

coincides with the dashed curve. The dramatically different behavior in  $Z_{1D}T$  of 5 nm Bi nanowires relative to that of the larger diameter wires is due to the subband crossing of  $\varepsilon_{h(T)}^{(0)}$  and  $\varepsilon_{h(L)}^{(0)}$  in trigonal Bi nanowires of very small  $d_w$ . For Bi nanowires oriented along the trigonal direction, the  $T$ -point holes have the smallest effective mass components ( $\sim 0.059m_0$ ) in the confined directions (the binary and the bisectrix directions), while the carriers in the  $L$ -point pockets have one of the largest effective mass components ( $\sim 0.11m_0$ ) in the confined directions. Since band shifting due to the quantum confinement effect is approximately proportional to the inverse of the mass component in the confined directions,  $\varepsilon_{h(T)}^{(0)}$  will move downwards faster than  $\varepsilon_{h(L)}^{(0)}$  as  $d_w$  decreases. In addition, the nonparabolic band structure also tends to reduce the band shifting of the  $T$ -point holes because of the increasing effective masses away from the band edge. Therefore, at a certain wire diameter ( $\leq 6$  nm),  $\varepsilon_{h(T)}^{(0)}$  crosses  $\varepsilon_{h(L)}^{(0)}$ , and the highest valence subband is formed by the  $L$ -point holes. The suppression of the  $T$ -point holes with respect to  $\varepsilon_{h(L)}^{(0)}$  results in nearly symmetric conduction and valence bands, and the influence of the  $T$ -point holes is therefore negligible for the range of  $E_F$  of greatest interest [see Fig. 8(d)].

Figure 9 shows the calculated  $Z_{1D}T$  as a function of acceptor dopant concentrations  $N_a$  at 77 K for  $p$ -type trigonal Bi nanowires with different  $d_w$ , and the dashed curves show the results for the corresponding wires assuming no  $T$ -point holes. The results for 5 nm  $p$ -type Bi nanowires are depicted in the inset figure for clarity. We note that with the presence of  $T$ -point holes in addition to the  $L$ -point holes, the dopant concentrations  $N_a$  required for the optimal  $Z_{1D}T$  for 10 nm and 40 nm Bi nanowires are much higher than that for their  $n$ -type counterparts (see Fig. 5), and the optimized  $N_a$  are  $\sim 1.3 \times 10^{19} \text{ cm}^{-3}$  and  $6.2 \times 10^{18} \text{ cm}^{-3}$  for 10 nm and 40 nm nanowires, respectively.

For binary and bisectrix Bi nanowires, the  $T$ -point holes have identical subband structures due to symmetry. In these two wire orientations, the  $T$ -point holes have one of the smallest effective mass components along the transport direction and the largest mass component lying in the confined

plane. Since the thermoelectric performance for one band is roughly proportional to  $(m^*)^{-1/2}$ , where  $m^*$  is the effective mass along the transport direction, the  $T$ -point holes are more favorable for  $p$ -type thermoelectric applications in the binary and the bisectrix wires rather than for the trigonal wires, though still much inferior to the  $L$ -point carriers.

We also note that, unlike trigonal wires, the band crossing between  $\varepsilon_{h(T)}^{(0)}$  and  $\varepsilon_{h(L)}^{(0)}$  is not observed for the binary and bisectrix wires for wire diameters down to 5 nm.<sup>23</sup> This is due to the smaller band shifting for the  $T$ -point holes in binary and bisectrix wires owing to the heavier effective mass in the confined directions. Therefore, for 5 nm binary and bisectrix wires, the  $T$ -point holes still play a crucial role in determining the overall  $Z_{1D}T$  in the  $p$ -type range.<sup>23</sup> However, it should be pointed out that for binary wires, the band crossing of  $\varepsilon_{h(L)}^{(0)}$  and  $\varepsilon_{h(T)}^{(0)}$  is predicted for wire diameters slightly below 5 nm, so that  $n$ -type and  $p$ -type binary nanowires with ultrasmall wire diameters will have symmetric performance. As for bisectrix wires, such a band crossing is very unlikely, because the very small effective mass component of the  $L$ -point pockets ( $\sim 0.0023m_0$ ) in the confined directions will move the band edge of the  $L$ -point holes down much faster than that of the  $T$ -point holes.

In general, for Bi nanowires oriented in other directions (binary, bisectrix,  $[10\bar{1}1]$ , and  $[01\bar{1}2]$  directions), the  $T$ -point holes exhibit a similar adverse effect on the  $Z_{1D}T$  for trigonal Bi nanowires discussed above,<sup>23</sup> and a detailed study on these wire orientations can be found in Ref. 23. It is interesting to point out that, since the band structure would become symmetric if there were no  $T$ -point holes, the optimal  $Z_{1D}T$  and the corresponding acceptor concentration  $N_{a(opt)}$  for  $p$ -type Bi nanowires in this case can be referred to the values of  $n$ -type Bi nanowires in Table VII, except for large wire diameters ( $>40$  nm) where the optimal performance of  $n$ -type Bi nanowires are affected by the  $T$ -point holes. By comparing the results in Tables VII and VIII, we note that a significant enhancement in  $Z_{1D}T$  can be achieved if the  $T$ -point holes can be removed or suppressed to lie below the  $L$ -point holes. One possible approach to this is to introduce an appropriate amount of antimony (Sb) into Bi to form  $\text{Bi}_{1-x}\text{Sb}_x$  alloys.<sup>16</sup> It is observed that, for Sb concentrations  $0.075 < x < 0.18$ , the  $T$ -point holes will lie below the  $L$ -point valence band edge in energy,<sup>37</sup> and the superior properties of the  $L$ -point holes can be utilized for practical thermoelectric applications.

#### IV. CONCLUSIONS

In this paper, we presented a theoretical model for cylindrical Bi nanowires, which considers explicitly the aniso-

tropic carrier pockets and the nonparabolic features of the  $L$ -point bands in Bi. A numerical solution is developed to describe the subband structure of Bi quantum wires. The critical wire diameter  $d_c$  for the semimetal-semiconductor transition in Bi nanowires at 77 K is then calculated, which is found to be between 39 nm and 55 nm, depending on the crystal orientation of the wire axis. The comparison of our  $d_c$  (or wire widths  $a_c$ ) and those predicted by two previous approximation models shows that significant discrepancies are caused by the anisotropic carrier pockets in Bi when this anisotropy is not properly taken into account. Because of the  $T$ -dependent band structure in bulk Bi,  $d_c$  decreases with increasing  $T$ .

The thermoelectric figure of merit  $Z_{1D}T$  is investigated for Bi nanowires, based on the semiclassical transport model and the band structure model, and the results show that small diameter Bi nanowires ( $d_w \leq 10$  nm), when properly doped, are potentially good thermoelectric materials with  $Z_{1D}T > 1$ . The effect of the  $T$ -point holes on the thermoelectric performance has also been discussed, and it is found that  $Z_{1D}T$  can be significantly enhanced, especially for  $p$ -type nanowires, if the  $T$ -point holes are removed or suppressed, which can possibly be achieved by Sb doping.

In this paper, we have mainly focused on the theoretical study. Recently, temperature-dependent resistance measurements have been reliably performed for as-prepared and deliberately doped Bi nanowire arrays of different diameters. The experimental results are consistent with the predictions based on the theoretical model developed in this communication. A detailed comparison is given in Ref. 11. However, the measurements of other transport properties of Bi nanowires (such as the Seebeck coefficient and the thermal conductivity) are more challenging, and so far, no experimental  $ZT$  values for Bi nanowires systems are available to the authors' knowledge. Efforts are being made to improve the measurements of these quantities so that reproducible experimental results can be obtained and the experimental  $ZT$  values of Bi nanowires can be determined.

#### ACKNOWLEDGMENTS

The authors thank Dr. G. Dresselhaus, Dr. J. Heremans of Delphi Corp., S. B. Cronin, and O. Rabin for valuable suggestions on the band structure calculations. They are also grateful to Professor G. Chen at UCLA for fruitful discussions on low-dimensional thermal conductivity issues. The support from MURI Subcontract No. 0205-G-7A114-01, NSF Grant No. DMR-98-04734, and U.S. Navy Contract No. N00167-92-K005 are gratefully acknowledged.

\*E-mail address: millie@mgm.mit.edu

<sup>1</sup>A. Gold and A. Ghazali, Phys. Rev. B **41**, 7626 (1990).

<sup>2</sup>B. Szafran, J. Adamowski, and S. Bednarek, Phys. Rev. B **61**, 1971 (2000).

<sup>3</sup>L. D. Hicks and M. S. Dresselhaus, Phys. Rev. B **47**, 16631 (1993).

<sup>4</sup>D. Schiferl and C. S. Barrett, J. Appl. Crystallogr. **2**, 30 (1969).

<sup>5</sup>R. T. Isaacson and G. A. Williams, Phys. Rev. **185**, 682 (1969).

<sup>6</sup>J. Heremans and O. P. Hansen, J. Phys. C **12**, 3483 (1979).

<sup>7</sup>Z. Zhang, J. Y. Ying, and M. S. Dresselhaus, J. Mater. Res. **13**, 1745 (1998).

<sup>8</sup>Z. Zhang, D. Gekhtman, M. S. Dresselhaus, and J. Y. Ying, Chem. Mater. **11**, 1659 (1999).

<sup>9</sup>T. E. Huber, M. J. Graf, and C. A. Foss Jr., in *Proceedings of the 18th International Conference on Thermoelectrics, Baltimore, MD*, edited by Gang Chen (IEEE, Piscataway, NJ, 1999), p. 558.

<sup>10</sup>J. Heremans and C. M. Thrush, Phys. Rev. B **59**, 12 579 (1999).

<sup>11</sup>Y.-M. Lin, S. B. Cronin, J. Y. Ying, M. S. Dresselhaus, and J.

- Heremans, Appl. Phys. Lett. **76**, 3944 (2000).
- <sup>12</sup>Z. Zhang, X. Sun, M. S. Dresselhaus, J. Y. Ying, and J. Heremans, Phys. Rev. B **61**, 4850 (2000).
- <sup>13</sup>X. Sun, Z. Zhang, and M. S. Dresselhaus, Appl. Phys. Lett. **74**, 4005 (1999).
- <sup>14</sup>Z. Zhang, X. Sun, M. S. Dresselhaus, J. Y. Ying, and J. Heremans, Appl. Phys. Lett. **73**, 1589 (1998).
- <sup>15</sup>X. Sun, Y. M. Lin, S. B. Cronin, M. S. Dresselhaus, J. Y. Ying, and G. Chen, in *Proceedings of the 18th International Conference on Thermoelectrics, Baltimore, MD*, edited by Gang Chen (IEEE, Piscataway, NJ, 1999), p. 394.
- <sup>16</sup>N. B. Brandt, S. M. Chudinov, and V. G. Karavaev, Zh. Éksp. Teor. Fiz **61**, 689 (1971) [Sov. Phys. JETP **34**, 368 (1972)].
- <sup>17</sup>J. Heremans, C. M. Thrush, Y.-M. Lin, S. Cronin, Z. Zhang, M. S. Dresselhaus, and J. F. Mansfield, Phys. Rev. B **61**, 2921 (2000).
- <sup>18</sup>J. Heremans, C. M. Thrush, Z. Zhang, X. Sun, M. S. Dresselhaus, J. Y. Ying, and D. T. Morelli, Phys. Rev. B **58**, R10 091 (1998).
- <sup>19</sup>K. Liu, C. L. Chien, P. C. Searson, and Y. Z. Kui, Appl. Phys. Lett. **73**, 1436 (1998).
- <sup>20</sup>N. W. Ashcroft and N. D. Mermin, *Solid State Physics* (Holt, Rinehart and Winston, New York, 1976), Appendix E.
- <sup>21</sup>V. S. Édel'man, Adv. Phys. **25**, 555 (1976).
- <sup>22</sup>B. Lax and J. G. Mavroides, in *Solid State Physics*, edited by F. Seitz and D. Turnbull (Academic Press, New York, 1960), Vol. 11, pp. 261–400.
- <sup>23</sup>Y.-M. Lin, Master's thesis, Massachusetts Institute of Technology, 2000.
- <sup>24</sup>X. Sun, Ph.D. thesis, Massachusetts Institute of Technology, 1999.
- <sup>25</sup>C. F. Gallo, B. S. Chandrasekhar, and P. H. Sutter, J. Appl. Phys. **34**, 144 (1963).
- <sup>26</sup>M. P. Vecchi and M. S. Dresselhaus, Phys. Rev. B **10**, 771 (1974).
- <sup>27</sup>N. W. Ashcroft and N. D. Mermin, *Solid State Physics* (Holt, Rinehart and Winston, New York, 1976), Chap. 13.
- <sup>28</sup>S. G. Walkauskas, D. A. Broido, K. Kempa, and T. L. Reinecke, J. Appl. Phys. **85**, 2579 (1999).
- <sup>29</sup>C. Kittel, *Introduction to Solid State Physics*, 7 ed. (Wiley, New York, 1996), Chap. 5.
- <sup>30</sup>L. D. Hicks and M. S. Dresselhaus, Phys. Rev. B **47**, 12 727 (1993).
- <sup>31</sup>H. J. Goldsmid, *Thermoelectric Refrigeration* (Plenum, New York, 1964).
- <sup>32</sup>N. W. Ashcroft and N. D. Mermin, *Solid State Physics* (Holt, Rinehart and Winston, New York, 1976), Chap. 16.
- <sup>33</sup>G. A. Saunders and Z. Sümengen, Proc. R. Soc. London, Ser. A **329**, 453 (1972).
- <sup>34</sup>G. K. White, J. Phys. C **5**, 2731 (1972).
- <sup>35</sup>K. Walther, Phys. Rev. **174**, 782 (1968).
- <sup>36</sup>Y. Eckstein, A. W. Lawson, and D. H. Reneker, J. Appl. Phys. **31**, 1534 (1960).
- <sup>37</sup>N. B. Brandt, V. V. Moshchalkov, and S. M. Chudinov, Zh. Éksp. Teor. Fiz. **74**, 1829 (1977) [Sov. Phys. JETP **47**, 953 (1977)].